

Thermal wave analysis of contact damage in ceramics: Case study on alumina

Lanhua Wei^{a)} and Brian R. Lawn

*Materials Science and Engineering Laboratory, National Institute of Standards and Technology,
Gaithersburg, Maryland 20899-0001*

(Received 29 March 1995; accepted 5 December 1995)

Thermal waves are used to image damage accumulation digitally beneath Hertzian contacts in ceramics. Alumina ceramics over a range of grain size 3–48 μm are used in a case study. The nature of the images changes with increasing alumina grain size, reflecting a transition in damage mode from well-defined cone fracture in the finer-grain materials to distributed subsurface microfracture in the coarser-grain materials. Quantitative determinations of microcrack densities are evaluated in the latter case by deconvoluting thermal diffusivities from the image data. These determinations confirm the grain-size dependence of degree of damage predicted by fracture mechanics models. Potential advantages and disadvantages of thermal waves as a route to damage characterization in ceramic systems are discussed.

I. INTRODUCTION

Thermal waves are proving to be a useful means of detecting and analyzing damage in brittle materials, notably ceramics.^{1–5} A particularly versatile technique uses lasers to generate and detect the thermal waves, and scans specimens to produce point-by-point images of the defect structures.^{6,7} Macroscopic cracks are most amenable to imaging in this way, because of their effectiveness in interrupting heat flow.^{1–3} Also amenable are microfractures, where individual events may be microscopic, but where integrated effects over a damage volume can manifest themselves as significant damage accumulation. The kind of information attainable from thermal wave analysis is both qualitative and quantitative: qualitative, by mapping microcrack distributions, either surface or subsurface^{3,5}; quantitative, by measuring point-by-point thermal diffusivity within the damage zone, and thereby determining microcrack densities.^{4,8}

Thermal wave analysis is especially useful for studying damage accumulation in Hertzian contact loading of ceramics.^{3,5,9–16} As the ceramics are made more heterogeneous (coarser grains, weaker internal interfaces, higher internal stresses), and thereby tougher,¹⁷ the damage undergoes a fundamental transition from a single macroscopic cone crack outside the contact area to a distributed zone of microfracture below the contact.¹¹ Preliminary studies using thermal waves as

an adjunct tool to map subsurface Hertzian damage in silicon nitride³ and zirconia⁵ have provided insights into the fundamental nature of such damage transitions.

In the present paper we present a more critical examination of thermal wave analysis as a tool for investigating damage accumulation in heterogeneous ceramics. Our approach will be to focus more on the scope of the methodology as a diagnostic and quantitative route to damage analysis, and less on experimental detail. We will illustrate the critical role of microstructure on damage accumulation with a Hertzian case study on aluminas covering a broad range of grain sizes. Thermal wave images of the contact sites will be used to provide diagnostic information on the nature and distribution of surface and subsurface fracture damage. A procedure for determining densities of damage from a thermal diffusivity analysis of the data, and for evaluating corresponding microcrack sizes in terms of fracture mechanics models, will also be outlined.

II. THERMAL WAVE IMAGING OF HERTZIAN CONTACT DAMAGE

A. Hertzian contact damage of alumina

Alumina provides an ideal model ceramic system for highlighting microstructural effects in damage accumulation. We choose a set of well-characterized aluminas from a previous study of the role of grain size on toughness properties.¹⁸ Specifically, the set includes grain sizes 3, 9, 15, 21, 35, and 48 μm (linear intercept

^{a)}Guest Scientist, on leave from Department of Physics and Astronomy, Wayne State University, Detroit, Michigan 48201.

evaluation).¹⁸ Experimental observations of Hertzian contact damage using optical microscopy,¹⁰ along with a theoretical analysis using fracture mechanics,¹⁹ have been reported for this material system.

The Hertzian contact test itself is simple to perform. An especially useful specimen configuration for investigating subsurface damage makes use of a "bonded interface."^{10,12} In this arrangement, two polished half-blocks are glued together at their sides with adhesive, and indentations are made along the interface trace on the top surface. In our experiments on such specimens, indentations are made with a tungsten carbide sphere of radius 3.18 mm at peak load $P = 2000$ N, corresponding to a mean pressure $P/\pi a^2 = 8.0$ GPa over the contact radius a .¹⁰ The half-blocks are then separated by immersion in solvent and gold-coated for viewing in the optical microscope using Nomarski illumination.

After optical characterization, the same bonded-interface alumina specimens are examined by thermal wave imaging.

B. Thermal wave "mirage" technique

A schematic of the thermal wave imaging technique used in the present work is shown in Fig. 1.¹⁷ The specimen surface is irradiated with a chopped (argon-ion) laser heating beam at normal incidence, and probed with a second (helium-neon) laser probe beam at grazing incidence. Periodic spatial and temporal temperature fluctuations, i.e., thermal waves, are generated in the irradiated specimen. The diffusivity of the heat in the

material away from the incident site is highly sensitive to the local defect structure. This sensitivity is manifested as variations in the near-surface atmospheric heating, which in turn shows up as variations in the refracted probe beam ("mirage" effect). A position detector monitors the probe beam deflections.

In the experiments to be described here, the setup is operated in an imaging mode. The laser beams are directed at the same spot within the specimen surface plane, and the specimen is scanned through the two fixed beams via *X-Y* actuators (Fig. 1). The heating beam is operated at a chopping frequency of 500 Hz, corresponding to a thermal diffusion length ≈ 100 μm in alumina.⁷ The probe beam deflections are recorded at each step on a data acquisition system. These data are then digitally processed to generate a thermal image of the defect content.^{6,7} One may deconvolute local thermal diffusivity values from the magnitude and phase of the probe beam deflection for each pixel in the image using heat diffusion equations²⁰ to convert the information into a point-by-point "diffusivity map."⁸ Because of the highly damped nature of thermal waves, the lateral resolution in the image is determined primarily by the specimen scan step (image pixel size) and the diameters of the heating and probe beam, but is insensitive to the thermal diffusion length.²¹ Accordingly, we use either a raster step size 10 μm and heating beam diameter 15 μm ("higher" resolution), or a step size 20 μm and heating beam diameter 30 μm ("lower" resolution); the probe beam diameter is kept constant at 15 μm . The price of a higher resolution is a longer scan time.

III. EXPERIMENTAL RESULTS

Figure 2 shows optical micrographs of the half-surface and subsurface Hertzian contact damage for each of the alumina grain sizes.¹⁰ Note the progressive transition from well-defined macroscopic cone crack at the lower grain sizes to distributed microscopic subsurface damage at the higher grain sizes. The generation of the subsurface damage has been documented as a two-stage process^{9,10,19}: stage 1 is the formation of closed "shear faults," intragrain twins in the case of alumina [most evident in Figs. 2(e) and 2(f)], within the subsurface compression-shear field; stage 2 is the nucleation of open intergrain microcracks within the local tensile stress concentrations at the ends of the constrained shear faults. Because the first of these stages is shear driven, the onset of subsurface damage occurs at some depth below the contact axis, where the shear stresses attain their maximum value.^{9,22-25}

Figure 3 is a thermal wave image of the Hertzian damage pattern for the 3 μm grain size alumina, scanned under the high resolution conditions cited above (Sec. II.B). The same broadscale cone crack

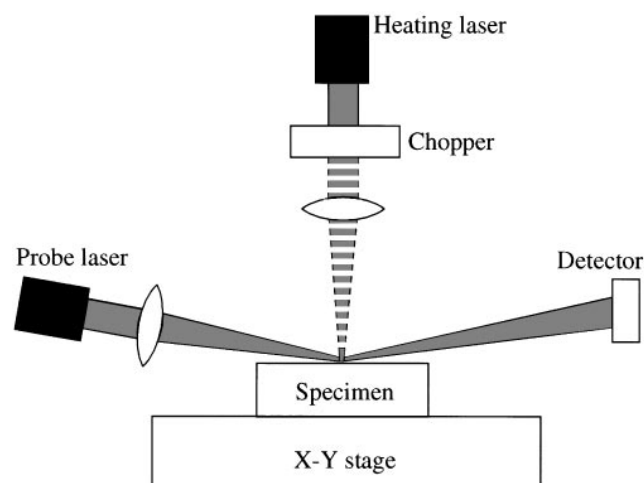


FIG. 1. Schematic of thermal wave setup. Chopped heating laser beam induces thermal waves in solid below incident spot; probe laser beam detects variations in atmospheric heating above spot. Specimen is scanned to produce thermal wave image of defect content in specimen.

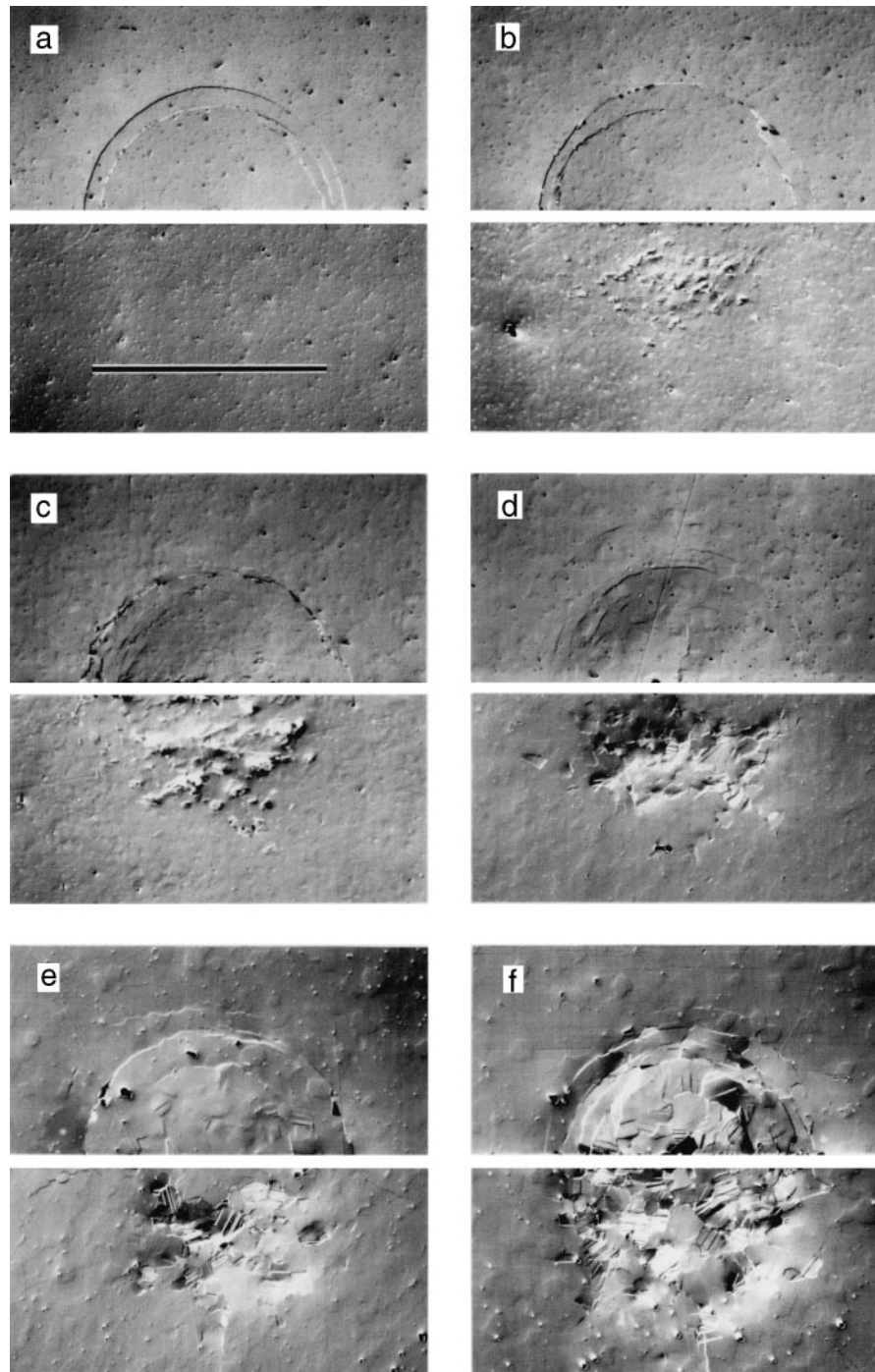


FIG. 2. Nomarski interference optical micrographs of Hertzian contact damage in alumina, grain sizes (a) 3, (b) 9, (c) 15, (d) 21, (e) 35, and (f) 48 μm , half-surface (upper) and section (lower) views from bonded-interface specimen. Indentations produced with WC sphere, radius 3.18 mm, load 2000 N, corresponding to peak contact pressure 8 GPa. Marker indicates contact diameter $2a = 550 \mu\text{m}$.¹⁰

features seen in the corresponding optical micrograph, Fig. 2(a), are apparent. There is no indication of any accompanying subsurface deformation in this image; 3 μm lies below the threshold grain size for twin-initiated microcrack initiation at the prescribed contact pressure in alumina^{10,19}; twins themselves, if present, are

“closed” defects and therefore unlikely to interrupt the heat flow significantly.³ Note that we can readily resolve three concentric cone crack segments spaced $\approx 20 \mu\text{m}$ apart at right in the half-surface view in Fig. 3.

To image the subsurface microfracture damage that is more representative of the larger grain sizes it is no

longer necessary to insist on high resolution, since we are now concerned more with the integrated effect of damage accumulation over the contact zone than with the imaging of individual defects. Indeed, lower resolution conditions help to smooth out local fluctuations in the point-by-point data, and thus enable a more reliable evaluation of average thermal diffusivities. Moreover, using the lower resolution conditions cited above increases the raster step size by a factor of two and hence decreases the scan time per specimen by a factor of four. Accordingly, we show in Fig. 4 lower resolution images for each of the alumina grain sizes. Comparison of the surface view in Fig. 4(a) with its higher-resolution counterpart in Fig. 3 reveals considerable smearing out of the cone crack traces. The transition from macroscopic cone fracture to distributed microfracture damage with increasing grain size seen in the optical micrographs in Fig. 2 is evident again in the thermal wave images. Also evident in the section images is a progressive expansion of the subsurface damage zone toward the top surface, so that ultimately for 48 μm grain size [Fig. 4(f)] the damage is readily detectable in the surface image. For 35 μm grain size [Fig. 4(e)], damage is still detectable in the surface image, if to a lesser extent, even though there is no indication that the microcrack zone extends to the surface in the corresponding optical view [Fig. 2(e)]. For intermediate grain sizes, 9 to 21 μm [Figs. 4(b)–4(d)], surface imaging alone is *not* able to detect the presence of the subsurface damage. This indicates a certain depth of thermal wave sensitivity, ≈ 30 μm in the present case, governed in part by the thermal diffusion length, but strongly diminished by an additional (r^{-1}) falloff in spherical wave intensity.²¹ Other factors, such as signal-to-noise ratio and defect size, also contribute to this sensitivity.

IV. QUANTITATIVE ANALYSIS OF DAMAGE

Thermal wave imaging provides a basis for quantitative evaluations of accumulated damage, specifically

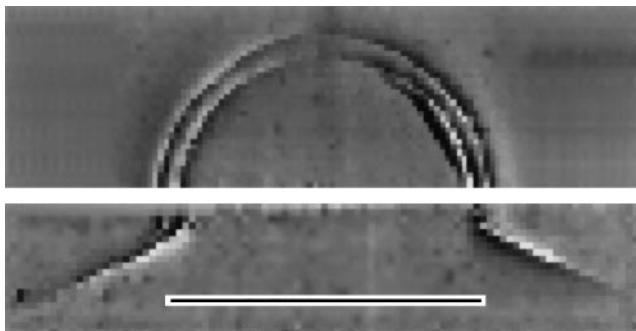


FIG. 3. Thermal wave images, half-surface and section views, for alumina of grain size 3 μm [cf. Fig. 2(a)]. Higher resolution conditions (frequency 500 Hz, raster step size 10 μm , heating beam spot diam 15 μm). Marker indicates contact diameter $2a = 550$ μm .

microcrack density, via local diffusivity measurements. As indicated in Sec. II.B, it is possible to deconvolute a thermal diffusivity α_i for any i th pixel in the digitized images in Fig. 4. In the present work we use an algorithm to average the quantity α_i/α_0 over all such pixels within a nominal damage area, where α_0 is the background diffusivity outside the damage area. For the section views in Fig. 4, the nominal damage area is taken as $\pi a^2/2$ where a is the contact radius (see inset, Fig. 5), so that for a linear pixel dimension λ the total number of “active” pixels is $n = \pi a^2/2\lambda^2$. We note that this procedure of averaging over the damage zone is more representative of the net damage accumulation than that used in earlier studies.^{3,4} There the evaluation was made by fixing the heating beam and specimen, scanning the probe beam across the heated spot to obtain a deflection profile,⁷ and deconvoluting the diffusivity assuming a uniform microcrack density. The present improved averaging procedure is especially pertinent to the damage zones for the larger grain sizes in Fig. 2, where the correspondingly larger scale of the individual cracks is likely to reflect in an exaggerated point-to-point scatter in the thermal signal.

The average crack density D over the damage zone may then be quantified using a relation derived from Hasselman²⁶ for the thermal conductivity of a solid with penny cracks of radius c and number density N per unit volume, making use of the proportionality between conductivity and diffusivity^{3,4} and summing over n pixels:

$$D = Nc^3 = (9/8n) \sum_i^n (\alpha_0/\alpha_i - 1) \quad (1)$$

for randomly oriented cracks.²⁶ The quantity D thus evaluated is plotted as a function of grain size l as the data points in Fig. 5 for the same alumina indentations shown in Fig. 4, for $\lambda = 30$ μm and $a = 275$ μm (see Figs. 2 and 3). These data are subject to a standard deviation error from indentation-to-indentation scatter, including an intrinsic uncertainty of $\approx 10\%$ from the repeatability of the thermal wave measurements for a given indentation.

These measurements may be compared with estimates of individual microcrack sizes from an earlier fracture mechanics model of the contact damage process.¹⁹ In that model, the sizes of microcracks initiated within the local tensile stress concentrations of intragrain twins at weak grain boundaries within the Hertzian subsurface stress field are calculated. Here we present just the essential results of those calculations in relation to our specific alumina materials and loading conditions, deferring formal details of the fracture mechanics to an appendix. The fracture mechanics formalism enables a computation of microcrack size as a function of grain size, $c(l)$. A plot

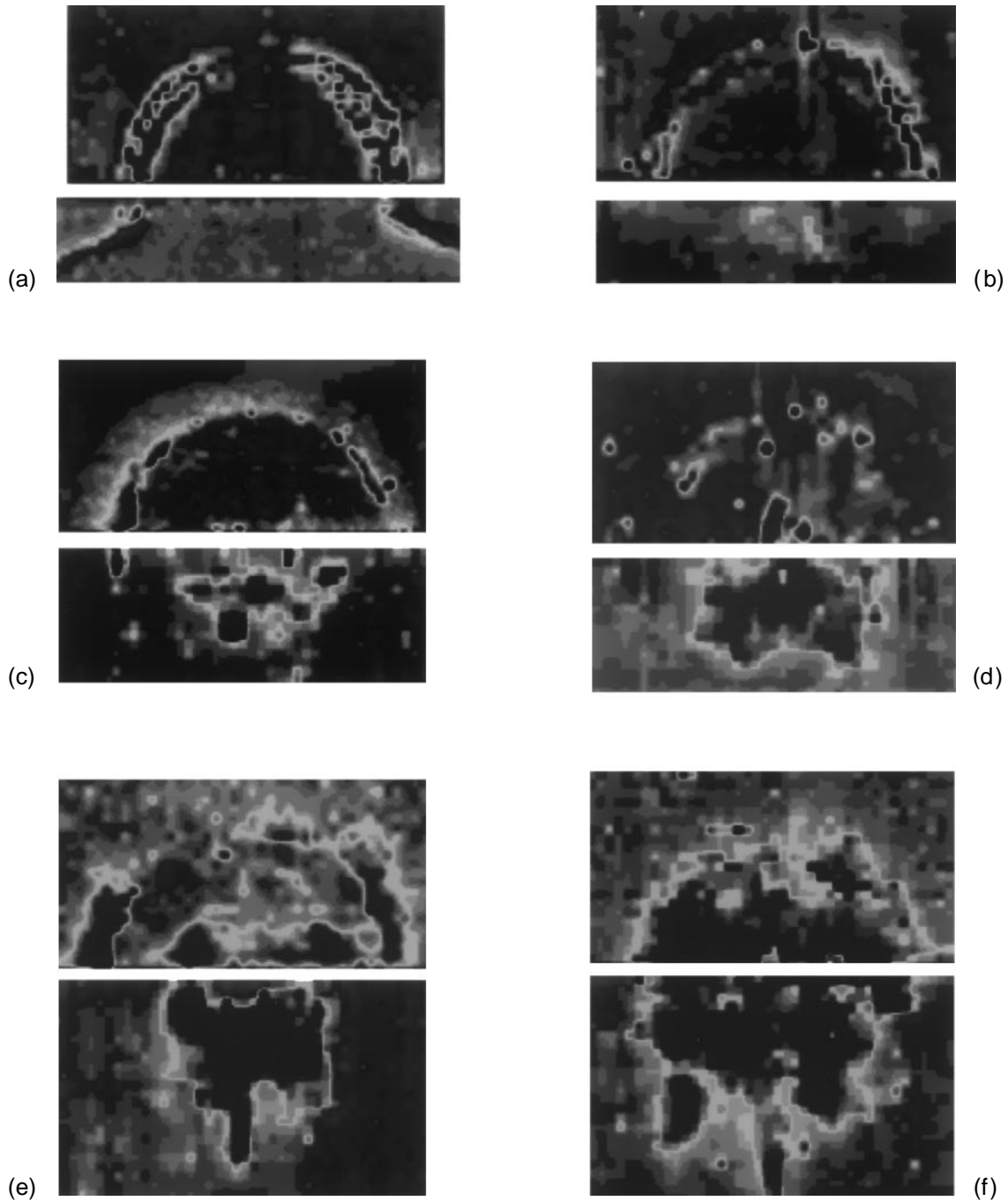


FIG. 4. Thermal wave images of alumina, half-surface and section views, for (a) 3, (b) 9, (c) 15, (d) 21, (e) 35, and (f) 48 μm . Lower resolution conditions (frequency 500 Hz, raster step size 20 μm , heating beam spot diam 30 μm). For scale, cf. Figs. 2 and 3.

of $c(l)$ for aluminas subjected to a peak contact pressure of 8 GPa (Fig. 2) is shown as the solid curve in Fig. 6. The data points in Fig. 6 are corresponding evaluations from the thermal wave measurements $D(l)$ in Eq. (1) with $N = 1/l^3$, i.e., assuming one facet microcrack per grain ("saturation" state, one twin per grain, one

microcrack per twin), giving an average crack size

$$c(l) = l[D(l)]^{1/3}. \quad (2)$$

The thermal wave evaluations are seen to scatter about the theoretical curve, indicating the capacity of the

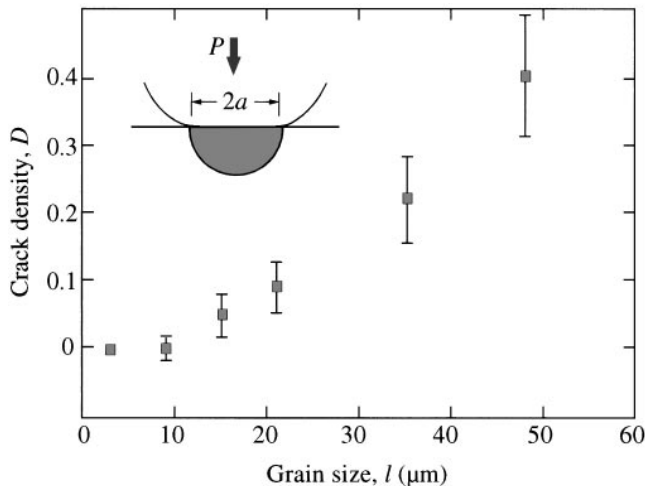


FIG. 5. Thermal wave evaluations of crack density as a function of grain size for alumina, averaged over damage zone (shaded area, inset).

technique to provide a quantitative measure of the microcrack size.

The zero value of crack size at the smallest grain size is consistent with the existence of a threshold for crack initiation (Sec. III), T in Fig. 6.¹⁰ The increasing slope of the curve at large grain sizes reflects the strong dependence of crack stress-intensity factors on the scale of the precursor shear fault that provides the driving force for microcracking.¹⁹

V. DISCUSSION

Our study on Hertzian contacts in alumina demonstrates the capacity of thermal wave techniques for detection and analysis of damage accumulation. The thermal wave images in Fig. 4 confirm most strikingly a fundamental change in fracture mode from tensile-driven macroscopic cone cracking to shear-driven multiple microcracking with increasing alumina grain size, as is apparent in the corresponding optical micrographs in Fig. 2. Analogous microstructural scaling effects have been reported in silicon nitride³ (although in that case over a much smaller range of grain size). Hence, thermal wave imaging can be a useful tool in the characterization of fracture-related damage in ceramics.

It should be emphasized, however, that the usefulness of thermal wave imaging is not restricted to confirmation of optical or other damage evaluation techniques. Thermal waves are highly sensitive to whether the damage elements are "open" or "closed," and when used in conjunction with optical microscopy are therefore able to distinguish conveniently between fracture and deformation components. Whereas open defects

(tensile cracks, pores) are highly effective in interrupting heat flow, closed defects (twins, slipped planes) are not. Thus in the images in Fig. 4 the contrast is attributable almost exclusively to the microcracks initiated by the precursor shear faults, and not to the shear faults themselves. This insensitivity to closed defects has been demonstrated more definitively in silicon nitride, where plastic deformation zones at subthreshold Hertzian contacts are clearly visible in optical micrographs but are correspondingly *invisible* in thermal wave images.³ It has also been demonstrated in zirconia, where again phase transformations are easily detected optically, but not thermally.^{5,15} The virtue of thermal wave imaging, therefore, is that it is sensitive principally to microcracks. This is of particular importance in the context of evaluating ceramics for structural applications, where cracks pose by far the most serious threat to material integrity. Accordingly, thermal wave imaging should be seen as complementary, not supplementary, to other damage characterization techniques.

A feature of the thermal wave technique is its amenability to quantitative analysis. In Fig. 6, the measured dependence of average crack size on grain size for our aluminas correlates with fracture mechanics predictions from microcrack extension models.¹⁹ There is some doubt concerning the assumptions underlying the analysis used to obtain the theoretical prediction in Fig. 6 (appendix), such as the supposition of one microcrack per grain and neglect of mutual interactions between adjacent microcracks. The values of coefficients used in the stress-intensity factor relations in the analysis are particularly open to error. Notwithstanding these sources of uncertainty, it is evident from Fig. 6 that the thermal wave methodology can provide useful information on damage accumulation trends, enabling comparison with fracture mechanics models.

Comparisons of the thermal wave evaluations of crack densities with alternative evaluations from elastic modulus measurements using a nanoindentation technique⁴ have provided useful additional validations of expected data trends in indented silicon nitride. Again, some discrepancies exist in absolute values from each technique.⁴ Despite these discrepancies, the thermal wave technique shows the same dependence of crack density with increasing contact load as its elastic modulus counterpart and, moreover, nondestructively.

A note may be made of the sensitivity (or insensitivity) of the thermal wave imaging to surface roughness. Is it possible that the image contrast in Fig. 4 is an artifact of surface uplift rather than a true measure of crack density? In previous work on silicon nitride,³ thermal wave images were obtained of a subsurface contact damage zone (analogous to Fig. 4) before and after polishing away $\approx 5 \mu\text{m}$ from the section surfaces. No detectable differences in the patterns could be discerned.

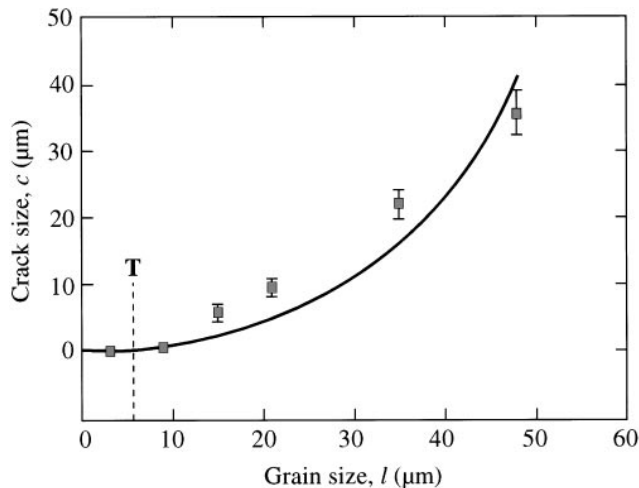


FIG. 6. Grain-facet microcrack size as a function of grain size in Hertzian damage zone in alumina, for indentation cycle with peak contact pressure 8.0 GPa. Solid curve is computation from fracture mechanics model (Appendix); data points are evaluations from thermal wave data (Fig. 5). T denotes threshold for crack initiation.

Recall also the previously mentioned observations on zirconia, in which microcrack-free damage zones from phase transformations showed no contrast in the thermal wave image, contrary to the observation of severe surface rumpling in the corresponding optical micrographs.⁵

The laser thermal wave technique advocated here does have some limitations. It may take several hours to generate a set of images (e.g., each image in Fig. 4 took about 1 h). Surface examination may not always be sufficient to detect subsurface damage, necessitating section views, as for the intermediate grain sizes in Fig. 4. Also, without making the raster step so small that the scan times become unmanageable, the resolution of the method is generally not high; thus, whereas we can resolve the surface cone cracks in Fig. 3, we cannot distinguish individual microcracks in Fig. 4. On the other hand, as we have pointed out, lack of resolution is not a major factor in evaluating cumulative damage.

Finally, we should emphasize that although we have focused here on a single-phase ceramic and single-cycle Hertzian damage, the usefulness of thermal wave analysis is expected to extend to a much broader range of contact and material configurations. Damage accumulation in cyclic contacts in relation to fatigue,^{5,9,13} and in sliding contacts in relation to wear,^{27,28} are pertinent examples. Thermal waves could be especially useful in characterizing damage in composite material systems.⁸

ACKNOWLEDGMENTS

The authors thank Fernando Guiberteau and Nitin P. Padture for providing the specimens shown in Fig. 2 and

for experimental assistance. This work was supported by the U.S. Air Force Office of Scientific Research.

REFERENCES

1. K. R. Grice, L. J. Inglehart, L. Favro, P. K. Kuo, and R. L. Thomas, *J. Appl. Phys.* **54**, 6245–6255 (1983).
2. J. Rantala, J. Hartikainen, and J. Jaarinen, *Appl. Phys. A* **50**, 465–471 (1990).
3. H. H. K. Xu, L. Wei, N. P. Padture, B. R. Lawn, and R. L. Yeckley, *J. Mater. Sci.* **30**, 869–878 (1995).
4. D. T. Smith and L. Wei, *J. Am. Ceram. Soc.* **78**, 1301–1304 (1995).
5. A. Pajares, L. Wei, B. R. Lawn, and D. B. Marshall, *J. Mater. Res.* **10**, 2613 (1995).
6. A. C. Boccard, D. Fournier, and J. Badoz, *Appl. Phys. Lett.* **36**, 130–132 (1980).
7. L. Wei, Ph.D. Thesis, Wayne State University, Detroit, MI (1993).
8. L. Wei and G. S. White, *J. Mater. Res.*, submitted.
9. F. Guiberteau, N. P. Padture, H. Cai, and B. R. Lawn, *Philos. Mag. A* **68**, 1003–1016 (1993).
10. F. Guiberteau, N. P. Padture, and B. R. Lawn, *J. Am. Ceram. Soc.* **77**, 1825–1831 (1994).
11. B. R. Lawn, N. P. Padture, H. Cai, and F. Guiberteau, *Science* **263**, 1114–1116 (1994).
12. H. Cai, M. A. Stevens Kalceff, and B. R. Lawn, *J. Mater. Res.* **9**, 762–770 (1994).
13. H. Cai, M. A. S. Kalceff, B. M. Hooks, B. R. Lawn, and K. Chyung, *J. Mater. Res.* **9**, 2654–2661 (1994).
14. N. P. Padture and B. R. Lawn, *J. Am. Ceram. Soc.* **77**, 2518–2522 (1994).
15. A. Pajares, F. Guiberteau, B. R. Lawn, and S. Lathabai, *J. Am. Ceram. Soc.* **78**, 1083–1086 (1995).
16. N. P. Padture and B. R. Lawn, *J. Am. Ceram. Soc.* **78**, 1431–1438 (1995).
17. B. R. Lawn, *Fracture of Brittle Solids* (Cambridge University Press, Cambridge, 1993).
18. P. Chantikul, S. J. Bennison, and B. R. Lawn, *J. Am. Ceram. Soc.* **73**, 2419–2427 (1990).
19. B. R. Lawn, N. P. Padture, F. Guiberteau, and H. Cai, *Acta Metall.* **42**, 1683–1693 (1994).
20. T. R. Anthony, W. F. Banholzer, J. F. Fleischer, L. Wei, P. K. Kuo, R. L. Thomas, and R. W. Pryor, *Phys. Rev. B* **42**, 1104–1111 (1990).
21. L. J. Inglehart, K. R. Grice, L. D. Favro, P. K. Kuo, and R. L. Thomas, *Appl. Phys. Lett.* **43**, 446–448 (1983).
22. R. M. Davies, *Proc. R. Soc. London A* **197**, 416–432 (1949).
23. D. Tabor, *Hardness of Metals* (Clarendon, Oxford, 1951).
24. M. V. Swain and B. R. Lawn, *Phys. Status Solidi* **35**, 909–923 (1969).
25. M. V. Swain and J. T. Hagan, *J. Phys. D: Appl. Phys.* **9**, 2202–2214 (1976).
26. D. P. H. Hasselman, *J. Composite Mater.* **12**, 403–407 (1978).
27. H. H. K. Xu and S. Jahanmir, *J. Am. Ceram. Soc.* **77**, 1388–1390 (1994).
28. H. H. K. Xu and S. Jahanmir, *J. Mater. Sci.* **30**, 2235–2247 (1995).
29. A. C. Fischer-Cripps and B. R. Lawn, *Acta Metall.* (in press).

VIII. APPENDIX: CALCULATION OF SIZE OF SHEAR-FAULT-INDUCED MICROCRACKS IN HERTZIAN CONTACT FIELD

Here we summarize the fracture mechanics formalism used to calculate microcrack sizes beneath Hertzian

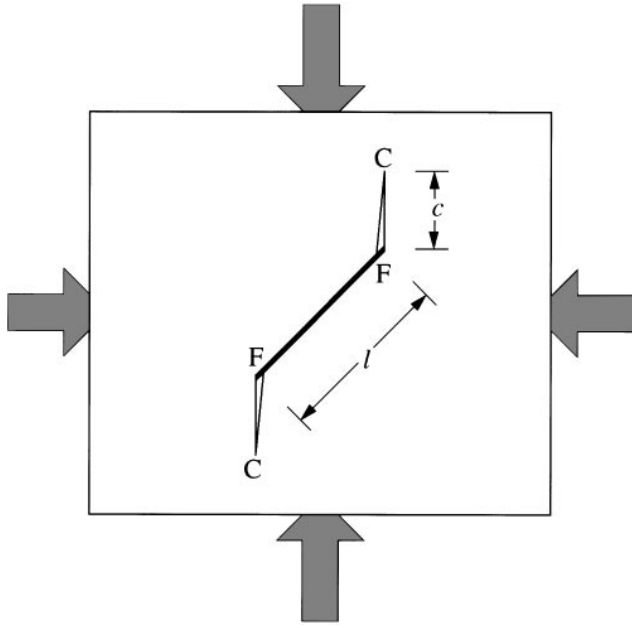


FIG. A1. Model for microcrack generation in compressive contact field. Figure shows volume element subject to principal stresses (arrows), containing shear fault FF with extensile microcracks FC at its ends.

contacts from an earlier model.¹⁹ The model centers on a volume element within the Hertzian subsurface compression stress field (Fig. A1). Faults FF inclined to the principal stresses generate extensile microcracks FC within local tensile stress concentrations at the constrained fault ends. In polycrystalline materials like alumina, the faults take the form of intergrain twins, and the ensuing microcracks form along weak grain boundaries. In other materials the faults may take on different forms,^{19,29} but the generic validity of the two-stage model remains intact.

The first stage in the modeling is to determine a constitutive relation for slip along the shear fault plane FF. The fault is driven by the resolved component of shear stress within the Hertzian field, and is resisted by internal cohesion. The second stage is to determine a stress-intensity factor $K(c)$ for microcrack extension along FC within the suppressed fields of the Hertzian field (compressive), the shear fault (locally tensile), and any internal mismatch stresses (tensile or compressive). Consideration of the system response through one entire cycle¹⁹ indicates that the microcracks initiate and extend during the loading half-cycle, driven by increasing Hertzian shear stresses on the fault planes, up to the peak contact pressure; extension continues during the unloading half-cycle, as the constraining Hertzian compressive stresses on the microcracks release.

From the standpoint of thermal wave evaluations, we concern ourselves exclusively with microcrack di-

mensions after completion of indentation, i.e., at contact pressure $p_0 = P/\pi a^2 = 0$ on unloading from a peak at $p_0 = p_0^*$. Then it is only the persistent field of the fault plus that from any internal residual (thermal expansion anisotropy) stress σ_R that need be retained in our evaluations. In the terminology of Ref. 19, these special considerations reduce the stress-intensity factor to $K(c) = K_F(c) + K_R(c)$, where subscripts F and R designate contributions from the fault and residual stresses, respectively. At equilibrium, the net stress-intensity factor may be written in familiar form:

$$K(c) = \sigma_F^S l^{1/2} f_F(c/l) + \sigma_R l^{1/2} f_R(c/l) = T_0, \quad (\text{A1})$$

with l the grain size and T_0 the grain boundary toughness. The term σ_F^S defines the shear-fault stress at peak load:

$$\sigma_F^S = \beta_F(p_0^* - p_F), \quad (\text{A2})$$

where β_F is the value of resolved Hertzian shear stress on the fault plane relative to p_0 , and p_F is the critical pressure at which an existent fault begins to slide during loading. The dimensionless quantities $f_F(c/l)$ and $f_R(c/l)$ define the crack-size dependence of the stress-intensity factor; writing $C = c + l/2$ as an effective crack dimension, we have¹⁹

$$f_F(C/l) = 2(C/\pi l)^{1/2} \times \{[1 - (1 - l^2/4C^2)^{1/2}] - [\nu/(2 - \nu)] \times [1 - (1 - l^2/4C^2)^{3/2}]\}. \quad (\text{A3a})$$

$$f_R(C/l) = 2(C/\pi l)^{1/2}(1 - l^2/4C^2)^{1/2} \quad (\text{A3b})$$

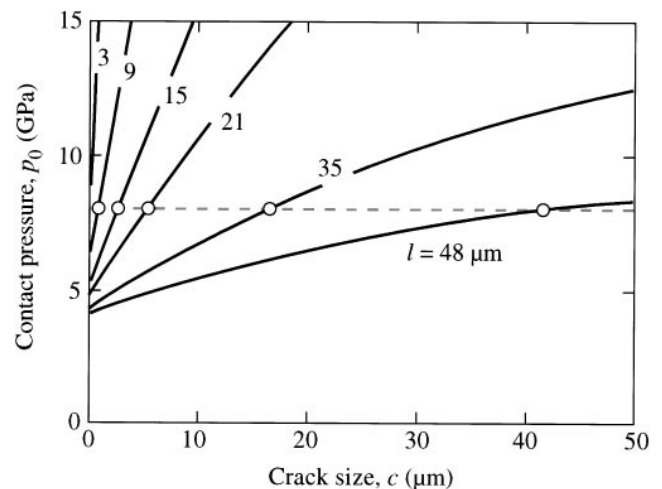


FIG. A2. Plot of peak contact pressure as a function of grain-facet microcrack size in alumina. Solid curves are functions for specific grain sizes used in Figs. 2 and 4. Horizontal dashed line is specific value of p_0^* used in Figs. 2 and 4. Note that no crack extension occurs at all at the smallest grain size, indicating a subthreshold configuration.

Once appropriate material parameters and contact conditions are specified, simultaneous solution of Eqs. (A1)–(A3) enables direct computations of the function $p_0^*(c)$ for any specified grain size l . For the alumina grain sizes used in Figs. 2 and 4, we make such computations using $p_F = 3.0$ GPa (data fit from Ref. 19), $\beta_F = 0.49$ (evaluated for a favorably oriented fault at point of maximum shear stress in Hertzian field), toughness $T_0 = 2.75$ MPa \cdot m^{1/2}, Poisson's ratio $\nu = 0.22$, and thermal expansion anisotropy stress $\sigma_R =$

+200 MPa.¹⁹ The results of the calculations are plotted as the solid curves in Fig. A2. The horizontal dashed line in this plot represents the peak contact pressure $p_0^* = 8.0$ GPa used in Figs. 2 and 4. The intersection points between the solid curves and horizontal dashed line then provide the equilibrium microcrack dimension c as a function of grain size l . Note that below a threshold grain size the shear fault does not initiate a microcrack, so there is no solution in that region. The ensuing $c(l)$ solution is plotted as the solid curve in Fig. 6.